Phase engineering of Cr_5Te_8 with colossal anomalous Hall effect

Bijun Tang[1], Xiaowei Wang[1], Mengjiao Han[2], Xiaodong Xu[3], Zhaowei Zhang[4], Chao Zhu[1], Xun Cao[1], Yumeng Yang[5], Qundong Fu[1], Jianqun Yang[3], Xingji Li[3], Weibo Gao[4], Jiadong Zhou[6]*, Junhao Lin[2]*, and Zheng Liu[1,7,8]**

[1]School of Materials Science and Engineering, Nanyang Technological University, Singapore 639798, Singapore.

[2]Department of Physics and Shenzhen Key Laboratory of Advanced Quantum Functional Materials and Devices, Southern University of Science and Technology, Shenzhen 518055, Guangdong, P. R. China

[3]School of Materials Science and Engineering, Harbin Institute of Technology, Harbin 150001, P. R. China

[4]Division of Physics and Applied Physics, School of Physical and Mathematical Sciences, Nanyang Technological University, Singapore 637371, Singapore.

[5]School of Information Science and Technology, ShanghaiTech University, Shanghai 201210, China

[6]Key Lab of advanced optoelectronic quantum architecture and measurement (Ministry of Education), Beijing Key Lab of Nanophotonics & Ultrafine Optoelectronic Systems, and School of Physics, Beijing Institute of Technology, Beijing 100081, China

[7]CINTRA CNRS/NTU/THALES, UMI 3288, Research Techno Plaza, 50 Nanyang Drive, Border X Block, Level 6, Singapore 637553, Singapore

[8]School of Electrical and Electronic Engineering, Nanyang Technological University, Singapore, 639798, Singapore

* Email: lxj0218@hit.edu.cn, jdzhou@bit.edu.cn, linjh@sustech.edu.cn, z.liu@ntu.edu.sg

The development of intrinsic ferromagnetism in two-dimensional (2D) limit is at the core of ultra-compact spintronic applications. However, direct synthesis of non-layered 2D magnets with strong ferromagnetic order is still in infancy. Here we report the phase-controllable synthesis of trigonal and monoclinic Cr_5Te_8 flakes via a facile chemical vapor deposition route. Both phases exhibit robust ferromagnetism with strong perpendicular anisotropy down to a few nanometers, as confirmed by both magneto-optical and

magnetotransport measurements. High Curie temperature up to 200 K is obtained by manipulating the phase structure and thickness. Remarkably, a colossal anomalous Hall effect is observed in the more distorted monoclinic Cr_5Te_8 with an enhanced anomalous Hall conductivity of 650 $\Omega^{-1}cm^{-1}$ and anomalous Hall angle of 5% achieved simultaneously. Our work paves the way for the scalable synthesis of 2D magnetic materials and highlights the great potential of Cr_5Te_8 for engineering future spintronic devices.

Introduction

Since the discovery of the ferromagnetism in the two-dimensional (2D) $Cr_2Ge_2Te_6$[1], CrI_3[2,3], and Fe_3GeTe_2 (FGT)[4,5], 2D magnets have been at the frontier of materials research[6]. To date, a number of fascinating behaviours of 2D magnets have been demonstrated, such as layer-dependent magnetism in CrI_3[2] and room-temperature ferromagnetism in FGT with ionic gating[5]. However, most reported materials possess limitations, including poor stability, complicated synthesis process, and less control over the sample size and thickness, hindering further study and applications. Therefore, the search for novel 2D magnets is not only an efficient strategy to investigate new physics and properties but also essential for next-generation spintronic applications.

Chromium-based chalcogenides (Cr_mX_n, where X = S, Se, and Te), are recently emerging as a class of key magnetic materials due to their tunable structural phases and magnetic properties via stoichiometric variations[7-11]. Of particular interest is that ferromagnetic ordering is present in all Cr_mTe_n compounds, which consist of alternating stacks of Cr-deficient and Cr-full layers along the c-direction that determines their fascinating magnetic properties[12-16]. It is predicted that the geometrically frustrated structure exists in Cr_5Te_8, which may give rise to nontrivial magnetic structure and rich transport properties such as topological Hall effect and large anomalous Hall effect (AHE)[17]. As one of the most important properties of ferromagnets, AHE results from magnetic-ordering and spin-orbit coupling (SOC)[18]. Large AHE is conducive to constructing next-generation non-dissipating electronic and spintronic devices, as the Joule

heating associated with the longitudinal current can be effectively suppressed. Therefore, Cr_5Te_8 appears to be an intriguing candidate to be explored among all Cr_mTe_n compounds. However, the non-layered structure of Cr_5Te_8 becomes an inherent obstacle to the preparation of its 2D counterpart in conventional exfoliation technique; thus, the production of 2D Cr_5Te_8 so far remains elusive[19,20], not to mention the phase-controllable synthesis. Therefore, developing a swift and effective approach to obtain 2D ferromagnetic Cr_5Te_8 with tunable structural morphology and magnetic properties is essential to explore and exploit the full potential of the intriguing 2D magnetism.

In this work, highly selective trigonal Cr_5Te_8 (tr-Cr_5Te_8) or monoclinic Cr_5Te_8 (m-Cr_5Te_8) crystals down to a few nanometers were prepared by a one-step chemical vapor deposition (CVD) method. The magnetic properties of the two phases were determined by magneto-optical measurements and extensive magnetotransport studies. Our results demonstrate that both tr-Cr_5Te_8 and m-Cr_5Te_8 crystals possess out-of-plane ferromagnetic order with Curie temperature (T_C) tuneable from 125 K to 200 K, depending sensitively on the sample phase and thickness. Importantly, anomalous Hall conductivity and anomalous Hall angle of m-Cr_5Te_8 reach 650 $\Omega^{-1}cm^{-1}$ and 5%, respectively, larger than typical itinerant ferromagnets. Density functional theory (DFT) calculations further revealed that the difference in ferromagnetism between the two phases arises from the structural distortion, which can be well interpreted by the magnetic anisotropy and Stoner criterion.

Results

Phase-controllable synthesis of 2D Cr_5Te_8. The experimental setup for the growth of 2D Cr_5Te_8 is schematically depicted in Supplementary Fig. 1. Briefly, chromium trichloride ($CrCl_3$) and tellurium (Te) powders were used as reactants to grow 2D Cr_5Te_8 flakes on the Si/SiO_2 substrate directly (see Methods). By controlling the experimental condition, either tr-Cr_5Te_8 or m-Cr_5Te_8 flakes can be preferentially obtained, whose corresponding atomic structures are presented in Fig. 1a,b. tr-Cr_5Te_8 belongs to *P-3m1* space group, while m-Cr_5Te_8 with a slightly

less Te concentration crystallizes into space group *C2/m*[21,22]. Identification and differentiation of these two structures are detailed in the microstructure analysis section.

We have calculated the formation energy difference between the two phases and found that the structure of m-Cr_5Te_8 is more distorted and thermodynamically less stable compared to that of tr-Cr_5Te_8 (details are elaborated in the last section). Such differences thus provide possibilities to achieve phase-selective growth of 2D Cr_5Te_8 by adjusting the synthesis environment (Supplementary Fig. 2). Higher growth temperature was used to obtain the thermodynamically more favorable tr-Cr_5Te_8[23]. Moreover, considering the slightly larger Te concentrations of tr-Cr_5Te_8 (61.5-62.0 at. % Te) than m-Cr_5Te_8 (59.6-61.5 at. % Te)[24], higher temperature is also conducive to the evaporation of Te precursors, ensuring a sufficient amount of Te reacted and incorporated into the Cr-Te matrix to obtain tr-Cr_5Te_8. On the other hand, fast cooling was adopted to facilitate the formation and preservation of the distorted m-Cr_5Te_8. Upon the completion of the reaction, the top cover of the furnace was opened immediately. Optical microscopy (OM) studies show two samples with distinct morphologies, which are in hexagonal and parallelogram shapes, respectively (Fig. 1c,e). Atomic force microscopy (AFM) analysis of these flakes exhibits flat surfaces with a height of 6 nm (Fig. 1d,f), indicating the ultra-thin nature. Due to lattice symmetry which governs the macroscopic morphology, the hexagonal and parallelogram flakes should correspond to tr-Cr_5Te_8 and m-Cr_5Te_8, respectively, which are precisely verified by the systematic atomic studies shown later.

To determine the chemical composition of the CVD-grown samples, we conducted X-ray photoelectron spectroscopy (XPS) and scanning electron microscopy energy-dispersive X-ray spectroscopy (SEM-EDS) measurements. The predominant signals of Cr and Te can be clearly identified from the XPS survey spectra and the resolved high-resolution spectra (Fig. 1g and Supplementary Fig. 3). Strong peaks located at around 573.0 eV and 583.4 eV represent the Te $3d_{5/2}$ and Te $3d_{3/2}$, respectively[25]. Peaks at around 576.6 eV and 586.8 eV correspond to the Cr $2p_{3/2}$ and Cr $2p_{1/2}$[26]. SEM-EDS measurement further verifies that the sample is composed of Cr and Te with an atomic ratio of ~5:8 (Supplementary Fig. 4). Two characteristic Raman peaks were found at around 117 and 137 cm^{-1} (under 532 nm laser excitation), which provides a quick

and efficient way to identify 2D Cr_5Te_8 in future work considering the abundant possible compositions of Cr_mTe_n family (Supplementary Figs. 5 and 6).

The facile polar reflective magnetic circular dichroism (RMCD) microscopy was conducted to investigate the magnetic property of the CVD-grown 2D Cr_5Te_8. As shown in Fig. 1h, both hexagonal and parallelogram Cr_5Te_8 flakes manifest rectangular hysteresis loops at the low temperature, which unambiguously indicate the ferromagnetism with perpendicular magnetic anisotropy. The large coercivity observed at around 2.5 K, together with the high coercivity field to saturation field ratio (H_C/H_S) of around 1, also suggests a large perpendicular anisotropy due to the strong SOC. As an important indicator of ferromagnetism, the T_C was further determined by plotting the remanent RMCD at zero magnetic field as a function of temperature (Fig. 1i and Supplementary Fig. 7). The temperature-dependent remanent RMCD signal was fitted by the functional form $A(1-T/T_C)^{\beta}$, where the A, T_C and β are simultaneous parameters. Compared to hexagonal Cr_5Te_8, parallelogram Cr_5Te_8 exhibits a larger magnetic response in terms of both H_C and T_C, which again suggests that different morphologies should originate from different phase structures and indicates a strong phase-dependent magnetic order in Cr_5Te_8 crystals. Moreover, thin flakes we studied show lower T_C than thick flakes (Supplementary Figs. 8 and 9), which is consistent with the previously reported metallic van der Waals ferromagnets[4-6].

Microstructure characterization and analysis. To further verify the phase-dependent morphology structure, we carefully examined the crystal structures of tr-Cr_5Te_8 and m-Cr_5Te_8 with the selected area diffraction (SAED) and atomic-resolution scanning transmission electron microscopy-high angle annular dark-field (STEM-HAADF) imaging. The crystal structure of both tr-Cr_5Te_8 and m-Cr_5Te_8 can be considered as Cr atoms intercalated in the van der Waals gap of $CrTe_2$, but in different ordered arrangements (Fig. 1a,b). For better illustration, the intralayer and interlayer Cr atoms are labelled as Cr_I and Cr_{II}, respectively, and highlighted by different colors (i.e., orange for Cr_I and green for Cr_{II}). For tr-Cr_5Te_8, the Cr_{II} atoms collectively intercalate underneath the Cr_I atomic columns with a 50% linear filling rate, resulting in a 2×2 supercell of $CrTe_2$ which doubles the lattice constant of $CrTe_2$ (the orange and green dashed parallelogram in Fig. 1a showing the periodic structure unit for Cr_I and Cr_{II}, respectively).

Therefore, such an ordered arrangement of Cr_{II} atoms superimposes a new periodicity with the same orientation but half the frequency of $CrTe_2$ lattice in the reciprocal space. This can be directly captured in the diffraction pattern viewed from the [001] zone axis of a hexagonal Cr_5Te_8 flake (Fig. 2a). After carefully indexing the lattice constants, we find the brightest {200} spot (highlighted by the orange hexagon) comes from the $CrTe_2$ backbones and the inner {100} supercell spots (highlighted by the green hexagon) originate from the ordered Cr_{II} atoms in the van der Waals gaps, consistent with our structural analysis.

Although m-Cr_5Te_8 shares the framework of $CrTe_2$, the ordering of Cr_{II} atoms is completely different from tr-Cr_5Te_8. The Cr_{II} atoms in two adjacent van der Waals gaps intercalate alternatively in different positions, which are classified as Cr_{II} and Cr'_{II}, respectively (side-view structure in Fig. 1b). Such alternating Cr_{II} intercalations generate misalignment of supercell patterns from Cr_{II} (Cr'_{II}) differed by one $CrTe_2$ unit cell between each layer, and also cause distortion of the supercell patterns as well as the $CrTe_2$ layered framework[27]. Fig. 2e shows the diffraction pattern of a parallelogram Cr_5Te_8 flake. The supercell spot (highlighted by the red circle) agrees well to the periodicity of intercalated Cr_{II} (Cr'_{II}) supercell patterns, but only two spots are revealed, indicating the two-fold rotational symmetry. Since the Cr_I atoms in the $CrTe_2$ framework also undergo severe anisotropic distortions (Fig. 1b), the hexagonal spots from $CrTe_2$ mostly retain but the specific lattice periodicity breaks the hexagonal symmetry, as highlighted by the yellow circle in Fig. 2e.

The elemental distribution and atomic ratio of tr-Cr_5Te_8 and m-Cr_5Te_8 were further revealed by EDS (Fig. 2b,f). The homogeneous distribution of Cr and Te elements throughout the entire flakes are shown in both phases, and the Cr:Te ratios are both around 0.62. Cross-sectional mappings further confirm the high quality of the synthesized Cr_5Te_8 without any phase segregation (Supplementary Figs. 10 and 11). STEM-HAADF imaging was further conducted to examine their atomic structures (Fig. 2c and g). The brighter atoms represent Te while the dimmer one corresponds to the Cr columns, as the contrast in HAADF image is directly related to the atomic number of the imaged species[28]. The projected Cr columns show slightly different contrast variations between two phases, owing to the different ordering of the intercalated Cr_{II} atoms. Simulated STEM images using corresponding phase models are consistent with the

experimental results (insets in Fig. 2c,g). To further examine the crystal structure of tr- and m-Cr_5Te_8, HAADF images were analyzed in detail by extracting the intensity line profiles (Fig. 2d,h). The intensity line profiles of tr-Cr_5Te_8 manifest alternating bright and dim contrast of adjacent Cr columns along two lattice directions inclined by 60˚, indicating a three-fold symmetric Cr intercalation consistent with the atomic model. In contrast, identical contrast of the adjacent Cr columns is revealed along the certain lattice direction in Fig. 2h, agreeing well with the two-fold symmetric Cr intercalation of the m-Cr_5Te_8. The experimental intensity profile in both phases matches well with the simulated STEM images, as shown in Fig. 2d,h. Therefore, from the atomic characterizations, the tr-Cr_5Te_8 flake is dominantly in hexagonal shape while m-Cr_5Te_8 in parallelogram, providing a facile means to distinguish the phase for the phase-dependent properties studies.

Magnetotransport measurement and AHE. In order to further analyze the ferromagnetic character of Cr_5Te_8 suggested by the RMCD measurement, samples with various thicknesses (i.e., 6 nm and 20 nm tr-Cr_5Te_8; 6 nm, 15 nm, and 20 nm m-Cr_5Te_8) were fabricated into devices to investigate the AHE through the magnetotransport measurement[5]. Figure 3a schematically illustrates the configuration of the hall bar device used for measurement. The temperature-dependent longitudinal resistance (R) of the 6 nm tr-Cr_5Te_8 and the 6 nm m-Cr_5Te_8 Hall bar devices are shown in Fig. 3b. OM and AFM analysis of the fabricated device are provided in Supplementary Fig. 12. To better interpret, resistances are normalized by their values at T = 250 K. The kinks in both R and their first temperature derivative (lower-right inset) at around 125 K and 150 K are characteristics of the established phase transition from paramagnetism to ferromagnetism. For both phases, the Hall resistance (R_{xy}) shows clear hysteresis loops at low temperatures as a function of the external magnetic field, $\mu_0 H$, applied perpendicular to the sample plane (Fig. 3c,d). Such hysteresis reflects the spontaneous magnetization and thus the long-range ferromagnetic order, which agrees well with the RMCD measurement. Raising the temperature introduces thermal fluctuations, and ferromagnetism eventually disappears above T_C. To fully elucidate the effect of sample phase and thickness on the ferromagnetism in 2D Cr_5Te_8, T_C is determined by examining the coercivity field (H_C) as a function of temperature (Fig. 3e,f, Supplementary Figs. 13 and 14). Under the same thickness (i.e., 6 nm), m-Cr_5Te_8

possesses a larger T_C than that of tr-Cr_5Te_8 (150 K vs 125 K, a detailed plot around T_C is presented in Supplementary Fig. 15). Additionally, it is clearly revealed that T_C decreases dramatically as the samples are thinned down for both phases, which is consistent with RMCD results and in line with most reported ferromagnets such as $Cr_2Ge_2Te_6$[1], FGT[4,5], $CrSe_2$[11], CrTe[29], $CrTe_2$[30], Cr_2Te_3[31]. The discovered thickness dependency is further investigated and supported by our theoretical calculations (details are elaborated in Supplementary Figs. 16 and 17).

To further evaluate the AHE in 2D Cr_5Te_8, the anomalous Hall conductivity (σ_{AHE}) and anomalous Hall angle (θ_{AHE}) were calculated and compared with various itinerant ferromagnets (Fig. 4a)[32,33]. The σ_{AHE} was obtained by inverting the resistivity matrix[34], $\sigma_{AHE} = \rho_{xy}/(\rho_{xx}^2 + \rho_{xy}^2)$. The θ_{AHE} was then determined by the ratio of σ_{AHE}/σ_{xx}, which measures the relative contribution of the anomalous Hall current with respect to the normal current. Notably, for most itinerant ferromagnets, σ_{AHE} and σ_{xx} are generally large or small at the same time, thereby leading to relatively smaller θ_{AHE}. In comparison, 2D Cr_5Te_8, especially the m-Cr_5Te_8, possesses superior anomalous Hall effect in terms of large σ_{AHE} and θ_{AHE}, which are 650 $\Omega^{-1}cm^{-1}$ and 5%, respectively. The σ_{AHE} of Cr_5Te_8 is also larger than that of FGT (650 vs 540 $\Omega^{-1}cm^{-1}$)[35]. Moreover, enhanced anomalous Hall response was found in Cr_5Te_8 with the reduced dimensionality, i.e., 2D Cr_5Te_8 has larger σ_{AHE} and θ_{AHE} than the bulk Cr_5Te_8 crystal[17].

To investigate the nature of the colossal Hall response in Cr_5Te_8, the σ_{AHE} of the samples discussed above was extracted and plotted against each device's σ^2_{xx} to study their scaling relation (Fig. 4b), which is generally adopted to identify the mechanism of AHE[18,36,37]. The varied σ^2_{xx} was due to the change of measurement temperature. A square dependency was observed in all the samples and can be well fitted by the previously reported quadratic scaling, which considers both skew scattering and intrinsic components of the AHE[34,38]:

$$\sigma_{AHE} = \alpha\sigma_{xx0}^{-1}\sigma_{xx}^2 + b \quad (1)$$

where α is the skew constant, σ_{xx0} is the residual conductivity, and b is the intrinsic σ_{AHE}. The side-jump contribution is precluded due to the observed linear relationship between the anomalous Hall resistivity (ρ_{AHE}) and the longitudinal resistivity (ρ_{xx}),[19,39] as shown in Supplementary Fig. 18. The extracted α and b are further analyzed in the inset of Fig. 4b. α

varies from 0.0202 to 0.0536, more than two orders of magnitude larger than Fe (0.00149) and Ni (0.0007)[38,40]. Figure 4c presents the σ_{AHE} versus σ_{xx} for all the materials discussed in Fig. 4a, spanning from the dirty regime (localized hopping regime) to the intrinsic regime, and eventually to the extrinsic regime (skew scattering regime)[32,34,37]. Grey lines show three σ_{AHE}/σ_{xx} ratios and their corresponding θ_{AHE} values. The scaling of AHE in Cr_5Te_8 with various thicknesses and phases is shown by the red dash line. A combination of the enhanced skew scattering parameter α and the quadratic scaling render 2D Cr_5Te_8 a promising candidate to realize large θ_{AHE} extrinsically within the reasonable σ_{xx} range. The quadratic dependence of σ_{AHE} on σ_{xx} means that θ_{AHE} can increase dramatically along with the increase of σ_{xx}, allowing a very large θ_{AHE} at practical σ_{xx}. For example, θ_{AHE} of 45° can be reached when σ_{xx} is around 2×10^5 $\Omega^{-1}cm^{-1}$, much smaller than the one required in other itinerant ferromagnets. An unrealistic σ_{xx} larger than 10^8 $\Omega^{-1}cm^{-1}$ is required for Fe to achieve the same θ_{AHE}. Even the recently reported KV_3Sb_5 with giant extrinsic AHE would require σ_{xx} of around 5×10^7 $\Omega^{-1}cm^{-1}$, two orders of magnitude larger than our 2D Cr_5Te_8[34].

Supplementary Table 1 summarizes the main features of Cr_5Te_8 compared against other reported Cr_mTe_n[14-17,29,41], including nonlayered CrTe, Cr_2Te_3, and layered $CrTe_2$. Among all the CVD-grown materials, Cr_5Te_8 manifests excellent performances considering both T_C and thickness (Supplementary Fig. 19). Though the thickness is more than eight times reduced, m-Cr_5Te_8 achieves comparable θ_{AHE} with the exfoliated $CrTe_2$ crystal[41]. In addition, the strong out-of-plane magnetization, i.e., perpendicular magnetic anisotropy, of Cr_5Te_8 offers superior qualities compared to the $CrTe_2$ with in-plane anisotropy for high density, fast access, and low power memory devices. The phase tunability of Cr_5Te_8 also adds another degree of freedom for manipulating ferromagnetism.

Theoretical insight into the magnetic order. To unveil the origin of the ferromagnetism in Cr_5Te_8 and the difference between the two phases, DFT calculations were adopted to investigate the magnetic ground state of 2D Cr_5Te_8. The calculated atomic structures of m-Cr_5Te_8 and tr-Cr_5Te_8 with structural relaxation are in line with our STEM measurements (Fig. 5a and Supplementary Fig. 20). The tr-Cr_5Te_8 has a lower formation enthalpy by 98.10 meV/atom, and the structure of m-Cr_5Te_8 is more distorted. For both phases, Cr atoms can be

classified into three types, which are distinguished by the structural distortion of the Cr-centered octahedra and colored in red (Cr1), green (Cr2), and blue (Cr3), respectively. It is verified that the spin-polarized states are originated from the *d* orbitals of Cr atoms. Figure 5b,c show the density of states (DOS) of spin-up and spin-down *d*-electron projected on the three types of Cr atoms. Governed by the distorted octahedra, significantly different spin splitting is exhibited in both phases. The monoclinic phase shows fully spin-polarized states with ferromagnetic ordering, while the spin splitting of Cr3 in the trigonal phase is opposite to that of Cr1 and Cr2, indicating the partial antiferromagnetic ordering in tr-Cr_5Te_8. The magnetic moments of Cr1, Cr2, and Cr3 are 3.73 μ_B, 3.73 μ_B, and 3.85 μ_B in the monoclinic phase, and 3.51 μ_B, 3.52 μ_B, and -3.67 μ_B in the trigonal phase, the direction of which easily points along the c-axis with the lowest energy (Fig. 5d,e). Governed by the structural distortion, m-Cr_5Te_8 shows noncolinear spin ordering, consistent with the previous report[42]. Notably, the average net magnetic moment of m-Cr_5Te_8 is 3.76 μ_B, much larger than that of tr-Cr_5Te_8 (2.06 μ_B), inferring that m-Cr_5Te_8 has stronger ferromagnetic coupled ordering than tr-Cr_5Te_8.

In order to reveal the underlying physics of the magnetic coupling difference between the two phases, the respective magnetic anisotropy was calculated, which is defined as $\Delta E = |E_\perp - E_\parallel|$, where $E_\perp$ and $E_\parallel$ represent the energy of the configuration with out-of-plane magnetic moments (c-axis) and in-plane magnetic moments (a-axis), respectively (Supplementary Fig. 21). The magnetic anisotropy of the m-Cr_5Te_8 is ΔE = 0.73 meV/Cr, larger than that of the tr-Cr_5Te_8 with ΔE = 0.62 meV/Cr, confirming that the c-axis is the easy magnetization direction, and m-Cr_5Te_8 has stronger magnetic stability. Additionally, the Stoner criterion was adopted to evaluate the ferromagnetic strength of the two structural phases. In principle, a d-electron metallic system reveals Stoner ferromagnetism if $(U'/N)\rho(E_F)>1$[43]. The $(U'/N)\rho(E_F)$ values of the m-Cr_5Te_8 and tr-Cr_5Te_8 are 1.14 and 1.01, respectively. Both phases meet the Stoner criterion, and the m-Cr_5Te_8 possesses stronger Stoner ferromagnetism. In short, the magnetic difference between m-Cr_5Te_8 and tr-Cr_5Te_8 can be well interpreted by the magnetic anisotropy and Stoner criterion, which is in good agreement with our experimental observations. The structural distortion dominates the strength of ferromagnetic coupling in 2D Cr_5Te_8, similar to our previously reported FeTe system[43].

Discussion

In this work, by tuning the growth temperature and controlling the cooling process, ultra-thin non-layered Cr_5Te_8 with selective trigonal and monoclinic phases have been synthesized using the one-step CVD method. Systematic characterizations including AFM, Raman, and STEM revealed the fine structural information of Cr_5Te_8 flakes and confirmed their high crystalline quality. RMCD study suggested that ferromagnetism with perpendicular magnetic anisotropy exists in both phases, which was further verified by magnetotransport Hall measurements. Apart from the higher T_C, colossal AHE was found in m-Cr_5Te_8 with anomalous Hall conductivity of 650 $\Omega^{-1}cm^{-1}$ and anomalous Hall angle of 5%. Among all the reported work on 2D magnets, our work is one of the few revealing the significant effect of phase structure on magnetic ordering on top of the well-studied thickness effect. The phase-dependent ferromagnetic response should be attributed to the different ferromagnetic coupling strengths arising from their different structural distortions, as revealed by the DFT calculations. Moreover, the optical image and Raman spectrum taken from the sample exposed in ambient conditions for two weeks suggest the desirable stability of thin Cr_5Te_8 flakes compared to other 2D magnets, rendering 2D Cr_5Te_8 an excellent candidate for comprehensive studies on correlated electron systems (Supplementary Fig. 22). Our work sheds light on the controllable growth of 2D magnetic material and establishes ferromagnetic Cr_mTe_n as a promising class of materials for fundamental research and future magnetoelectronic and spintronic applications.

Methods

CVD Synthesis of 2D Ferromagnetic Cr_5Te_8. $CrCl_3$ and Te powders were used as precursors, and Si/SiO_2 wafer was used as the substrate. A quartz boat loaded with Te powders was placed in the upstream zone. $CrCl_3$ powders were put into a ceramic boat and covered by a Si/SiO_2 substrate with the polishing surface down. The boat was then placed at the heating center of the 1-inch diameter quartz tube. A mixture of Ar and H_2 (100/5 sccm) was used as the carrier gas throughout the whole process. The growth temperature was set within the range of 670~730 ℃ with a ramp rate of 50 ℃ min^{-1} and maintained for 2 min for the growth of Cr_5Te_8.

For the thermodynamically more favorable tr-Cr_5Te_8, natural cooling is used. For m-Cr_5Te_8, fast cooling is adopted, where the top cover of the furnace is opened once the reaction is completed. A fan is also used for a fast-cooling process.

Raman, XPS, and SEM-EDS Characterization. A WITEC alpha 300R Confocal Raman system with 532 nm excitation laser was used to perform Raman and PL characterizations. Prior to the measurement, the system was calibrated with the Raman peak of Si at 520 cm^{-1}. To prevent the overheating of samples, laser powers were kept below 1 mW. A Kratos AXIS Supra spectrometer with a monochromatic Al K-alpha source was adopted to conduct XPS analysis. A 3.1 V bias was applied to the sample to prevent the charge build-up on the sample surface. The collected XPS spectra were calibrated with the binding energy of C1s at 284.8 eV. A JOEL JSM-7600F system with an accelerating voltage of 15 kV was used to perform the SEM-EDS characterization.

RMCD Measurement. A linearly polarized 633 nm HeNe laser was modulated by a PEM with a frequency of 50 kHz. The PEM retardation was set as λ/4. After the PEM, the laser beam was focused on the sample at normal incidence by an objective (Olympus MPLN50×, 0.75NA). The reflective light was collected by a photodetector and analyzed by a lock-in amplifier. The frequency of the lock-in amplifier was set as the same as the PEM. The RMCD measures the differential reflection between left and right circularly polarized light, whose magnitude is proportional to the magnetic moments of the Cr_5Te_8 sample.

STEM Characterization. HAADF-STEM imaging and EDS analysis were carried out on an FEI Titan Themis apparatus with an X-FEG electron gun and a DCOR aberration corrector operating at 300 kV. The convergent semi-angle for the incident probe was set at about 25 mrad.

Hall Device Fabrication and Measurements. The Si/SiO_2 substrate with the grown Cr_5Te_8 on top was first spin-coated with PMMA. The Electron-beam Lithography (Nova nanoSEM 230 with digital pattern generator Nabity-Nanometer Pattern Generation System (NPGS)) was then used to define the electrode patterns. After developing the pattern in Methyl Isobutyl Ketone (MIBK)/IPA, Kurt J. Lesker Nano 36 Thermal Evaporator was adopted to deposit metal

contacts. Hall measurements were conducted with six-terminal Hall bar structures using a Cryomagnetics cryostat with a current source/nanovoltmeter pair (Keithley 6221/2182A).

DFT Calculations. DFT calculations are performed using Vienna ab initio simulation package (VASP)[44,45] with the projector-augmented wave (PAW) pseudopotential and plane-wave basis set[46,47]. The Perdew-Burke-Ernzerhof in the framework of generalized gradient approximation (GGA-PBE) was adopted as exchange-correlation functional[48]. Gamma-centered k-point mesh of 18×21×12 and 18×18×24 was set for the monoclinic and trigonal phase in structural relaxation calculations and static self-consistent calculations. Structural relaxations were converged until the absolute force on each atom is less than 0.01 eV/Å. The electron relaxation convergence criterion was 10^{-6} eV. 800 eV is chosen for the plane-wave kinetic cutoff energy set in all calculations. Using a linear response method[49], the effective on-site Coulomb interaction energy for Cr d orbitals was self-consistently determined to U_{eff} = 5.95 eV for monoclinic phase and U_{eff} = 4.94 eV for trigonal phase applied to Dudarev's approach[50]. The SOC effect was also taken into account for determining the magnetic anisotropy.

Estimation of Stoner criterion. A 1×1×2 superlattice of trigonal phase is used to keep the same numbers of magnetic cell with the monoclinic phase. The definition of Stoner parameter is ST=$(U'/N)\rho(E_F)$[43], where U'=$<\epsilon_k>/m_d$. N equals 10 in this situation, representing the number of unit magnetism cells in two structural phases of Cr_5Te_8. $\rho(E_F)$ is the nonmagnetic total density of states of all d orbitals at Fermi level (Supplementary Fig. 23), i.e., 7.91 states/eV/Cr for the monoclinic phase and 7.79 states/eV/Cr for the trigonal phase. $<\epsilon_k>$ indicates the average splitting energy in band structure between the corresponding spin-up and spin-down bands at high symmetric k-points in the whole of Brillouin zoon. As shown in Supplementary Fig. 24, the splitting energy between the selected *d* bands is 5.43 eV for the monoclinic phase and 4.60 eV for the trigonal phase, respectively. m_d represents the average magnetic moments of d electrons on Cr atoms, i.e., 3.76 μ_B for the monoclinic phase and 3.54 μ_B for the trigonal phase.

Data availability

The data that support the findings of this study are available from the corresponding author upon reasonable request.

Code availability

The code for calculating Stoner parameter and spin ordering is available from the corresponding author upon reasonable request.

References

1 Gong, C. *et al.* Discovery of intrinsic ferromagnetism in two-dimensional van der Waals crystals. *Nature* **546**, 265-269 (2017).

2 Huang, B. *et al.* Layer-dependent ferromagnetism in a van der Waals crystal down to the monolayer limit. *Nature* **546**, 270-273 (2017).

3 Li, T. *et al.* Pressure-controlled interlayer magnetism in atomically thin CrI_3. *Nature materials* **18**, 1303-1308 (2019).

4 Fei, Z. *et al.* Two-dimensional itinerant ferromagnetism in atomically thin Fe_3GeTe_2. *Nature materials* **17**, 778-782 (2018).

5 Deng, Y. *et al.* Gate-tunable room-temperature ferromagnetism in two-dimensional Fe_3GeTe_2. *Nature* **563**, 94-99 (2018).

6 Gibertini, M., Koperski, M., Morpurgo, A. & Novoselov, K. Magnetic 2D materials and heterostructures. *Nature nanotechnology* **14**, 408-419 (2019).

7 Zhang, Y. *et al.* Ultrathin Magnetic 2D Single-Crystal CrSe. *Advanced Materials* **31**, 1900056 (2019).

8 Zhou, S. *et al.* Ultrathin non-van der Waals magnetic Rhombohedral Cr_2S_3: space-confined chemical vapor deposition synthesis and raman scattering investigation. *Advanced Functional Materials* **29**, 1805880 (2019).

9 Cui, F. *et al.* Controlled Growth and Thickness-Dependent Conduction-Type Transition of 2D Ferrimagnetic Cr_2S_3 Semiconductors. *Advanced Materials* **32**, 1905896 (2020).

10 Chu, J. *et al.* Sub-millimeter-scale growth of one-unit-cell-thick ferrimagnetic Cr_2S_3 nanosheets. *Nano letters* **19**, 2154-2161 (2019).

11 Li, B. *et al.* Van der Waals epitaxial growth of air-stable CrSe2 nanosheets with thickness-tunable magnetic order. *Nature Materials* **20**, 818-825 (2021).

12 Dijkstra, J., Van Bruggen, C., Haas, C. & de Groot, R. Electronic band-structure calculations of some magnetic chromium compounds. *Journal of Physics: Condensed Matter* **1**, 9163 (1989).

13 Dijkstra, J., Weitering, H., Van Bruggen, C., Haas, C. & De Groot, R. Band-structure calculations, and magnetic and transport properties of ferromagnetic chromium tellurides (CrTe, Cr_3Te_4, Cr_2Te_3). *Journal of Physics: Condensed Matter* **1**, 9141 (1989).

14 Wen, Y. *et al.* Tunable Room-temperature Ferromagnetism in two-dimensional Cr_2Te_3. *Nano Letters* **20**, 3130-3139 (2020).

15 Coughlin, A. L. *et al.* Near Degeneracy of Magnetic Phases in Two-Dimensional Chromium Telluride with Enhanced Perpendicular Magnetic Anisotropy. *ACS nano* (2020).

16 Meng, L. *et al.* Anomalous thickness dependence of Curie temperature in air-stable two-dimensional ferromagnetic 1T-$CrTe_2$ grown by chemical vapor deposition. *Nature communications* **12**, 1-8 (2021).

17 Wang, Y. *et al.* Magnetic anisotropy and topological Hall effect in the trigonal chromium tellurides Cr_5Te_8. *Physical Review B* **100**, 024434 (2019).

18 Nagaosa, N., Sinova, J., Onoda, S., MacDonald, A. H. & Ong, N. P. Anomalous hall effect. *Reviews of modern physics* **82**, 1539 (2010).

19 Liu, Y. & Petrovic, C. Anomalous Hall effect in the trigonal Cr_5Te_8 single crystal. *Physical Review B* **98**, 195122 (2018).

20 Zhang, X., Yu, T., Xue, Q., Lei, M. & Jiao, R. Critical behavior and magnetocaloric effect in monoclinic Cr_5Te_8. *Journal of Alloys and Compounds* **750**, 798-803 (2018).

21 Bensch, W., Helmer, O. & Näther, C. Determination and redetermination of the crystal structures of chromium tellurides in the composition range $CrTe_{1.56}$-$CrTe_{1.67}$: Trigonal di-chromium tri-telluride Cr_2Te_3, monoclinic penta-chromium octa-telluride Cr_5Te_8,

and the five layer superstructure of trigonal penta-chromium octa-telluride Cr_5Te_8. *Materials research bulletin* **32**, 305-318 (1997).

22 Lukoschus, K., Kraschinski, S., Näther, C., Bensch, W. & Kremer, R. Magnetic properties and low temperature X-ray studies of the weak ferromagnetic monoclinic and trigonal chromium tellurides Cr_5Te_8. *Journal of Solid State Chemistry* **177**, 951-959 (2004).

23 Wang, X. *et al.* Ultrathin FeTe nanosheets with tetragonal and hexagonal phases synthesized by chemical vapor deposition. *Mater Today* (2021).

24 Ipser, H., Komarek, K. L. & Klepp, K. O. Transition metal-chalcogen systems viii: The Cr-Te phase diagram. *Journal of the Less Common Metals* **92**, 265-282 (1983).

25 Tang, B. *et al.* Phase-Controlled Synthesis of Monolayer Ternary Telluride with a Random Local Displacement of Tellurium Atoms. *Advanced Materials* **31**, 1900862 (2019).

26 Biesinger, M. C. *et al.* Resolving surface chemical states in XPS analysis of first row transition metals, oxides and hydroxides: Cr, Mn, Fe, Co and Ni. *Applied Surface Science* **257**, 2717-2730 (2011).

27 Lasek, K. *et al.* Molecular Beam Epitaxy of Transition Metal (Ti-, V-, and Cr-) Tellurides: From Monolayer Ditellurides to Multilayer Self-Intercalation Compounds. *ACS nano* **14**, 8473-8484 (2020).

28 Krivanek, O. L. *et al.* Atom-by-atom structural and chemical analysis by annular dark-field electron microscopy. *Nature* **464**, 571-574 (2010).

29 Wang, M. *et al.* Two-dimensional ferromagnetism in CrTe flakes down to atomically thin layers. *Nanoscale* **12**, 16427-16432 (2020).

30 Zhang, X. *et al.* Room-temperature intrinsic ferromagnetism in epitaxial $CrTe_2$ ultrathin films. *Nature communications* **12**, 1-9 (2021).

31 Coughlin, A. L. *et al.* Near Degeneracy of Magnetic Phases in Two-Dimensional Chromium Telluride with Enhanced Perpendicular Magnetic Anisotropy. *ACS nano* **14**, 15256-15266 (2020).

32 Asamitsu, A. *et al.* Anomalous Hall effect and Nernst effect in itinerant ferromagnets. *Journal of magnetism and magnetic materials* **310**, 2000-2002 (2007).

33 Liu, E. *et al.* Giant anomalous Hall effect in a ferromagnetic kagome-lattice semimetal. *Nature physics* **14**, 1125-1131 (2018).

34 Yang, S.-Y. *et al.* Giant, unconventional anomalous Hall effect in the metallic frustrated magnet candidate, KV_3Sb_5. *Science advances* **6**, eabb6003 (2020).

35 Kim, K. *et al.* Large anomalous Hall current induced by topological nodal lines in a ferromagnetic van der Waals semimetal. *Nature materials* **17**, 794-799 (2018).

36 Miyasato, T. *et al.* Crossover behavior of the anomalous Hall effect and anomalous Nernst effect in itinerant ferromagnets. *Physical review letters* **99**, 086602 (2007).

37 Fujishiro, Y. *et al.* Giant anomalous Hall effect from spin-chirality scattering in a chiral magnet. *Nature communications* **12**, 1-6 (2021).

38 Tian, Y., Ye, L. & Jin, X. Proper scaling of the anomalous Hall effect. *Physical review letters* **103**, 087206 (2009).

39 Jiang, Z. *et al.* Magnetic anisotropy and anomalous Hall effect in monoclinic single crystal Cr_5Te_8. *Physical Review B* **102**, 144433 (2020).

40 Ye, L., Tian, Y., Jin, X. & Xiao, D. Temperature dependence of the intrinsic anomalous Hall effect in nickel. *Physical Review B* **85**, 220403 (2012).

41 Huang, M. *et al.* Colossal Anomalous Hall Effect in Ferromagnetic van der Waals $CrTe_2$. *ACS nano* (2021).

42 Huang, Z.-L., Kockelmann, W., Telling, M. & Bensch, W. A neutron diffraction study of structural and magnetic properties of monoclinic Cr5Te8. *Solid state sciences* **10**, 1099-1105 (2008).

43 Kang, L. *et al.* Phase-controllable growth of ultrathin 2D magnetic FeTe crystals. *Nature communications* **11**, 1-9 (2020).

44 Kresse, G. & Furthmüller, J. Efficient iterative schemes for ab initio total-energy calculations using a plane-wave basis set. *Physical review B* **54**, 11169 (1996).

45 Kresse, G. & Furthmüller, J. Efficiency of ab-initio total energy calculations for metals and semiconductors using a plane-wave basis set. *Computational materials science* **6**, 15-50 (1996).

46 Blöchl, P. E. Projector augmented-wave method. *Physical review B* **50**, 17953 (1994).

47 Kresse, G. & Joubert, D. From ultrasoft pseudopotentials to the projector augmented-wave method. *Physical review b* **59**, 1758 (1999).

48 Perdew, J. P., Burke, K. & Ernzerhof, M. Generalized gradient approximation made simple. *Physical review letters* **77**, 3865 (1996).

49 Cococcioni, M. & De Gironcoli, S. Linear response approach to the calculation of the effective interaction parameters in the LDA+ U method. *Physical Review B* **71**, 035105 (2005).

50 Dudarev, S., Botton, G., Savrasov, S., Humphreys, C. & Sutton, A. Electron-energy-loss spectra and the structural stability of nickel oxide: An LSDA+ U study. *Physical Review B* **57**, 1505 (1998).

Acknowledgments

Z.L. acknowledges the support from National Research Foundation Singapore programme NRF-CRP22-2019-0007 and NRF-CRP21-2018-0007. This research is also supported by the Ministry of Education, Singapore, under its AcRF Tier 3 Programme 'Geometrical Quantum Materials' (MOE2018-T3-1-002), AcRF Tier 2 (MOE2016-T2-1-131) and AcRF Tier 1 RG4/17 and RG7/18. This work is also supported by National Natural Science Foundation of China (Grant No. 11974156), Guangdong International Science Collaboration Project (Grant No. 2019A050510001), Guangdong Innovative and Entrepreneurial Research Team Program (Grant No. 2019ZT08C044), Shenzhen Science and Technology Program (No. KQTD20190929173815000), the Science, Technology and Innovation Commission of Shenzhen Municipality (No. ZDSYS20190902092905285), and also the assistance of SUSTech Core Research Facilities, especially technical support from Pico-Centre that receives support from Presidential fund and Development and Reform Commission of Shenzhen Municipality.

Author Contributions

B.T., X.W., M.H., and X.X. contributed equally to this work. Z.L., J.L., and J.Z. conceived and supervised the project. B.T. synthesized the sample and conducted AFM, XPS, SEM-EDS, and Raman characterizations. X.W. fabricated the devices and carried out the tranport measurements and AHE data analysis. M.H., C.Z., and J.L. performed the STEM measurement and data analysis. Z.Z. and W.G. conducted the RMCD measurements and data analysis. X.C. assisted with the FIB lithography. X.X., J.Y., and X.L. did the first-principle calculations. B.T., M.H., Z.Z., and X.X. co-wrote the manuscript. X.W., Y.Y., Q.F., J.Z., J.L., and Z.L. discussed the results and commented on the manuscript.

Competing interests

The authors declare no competing interests.

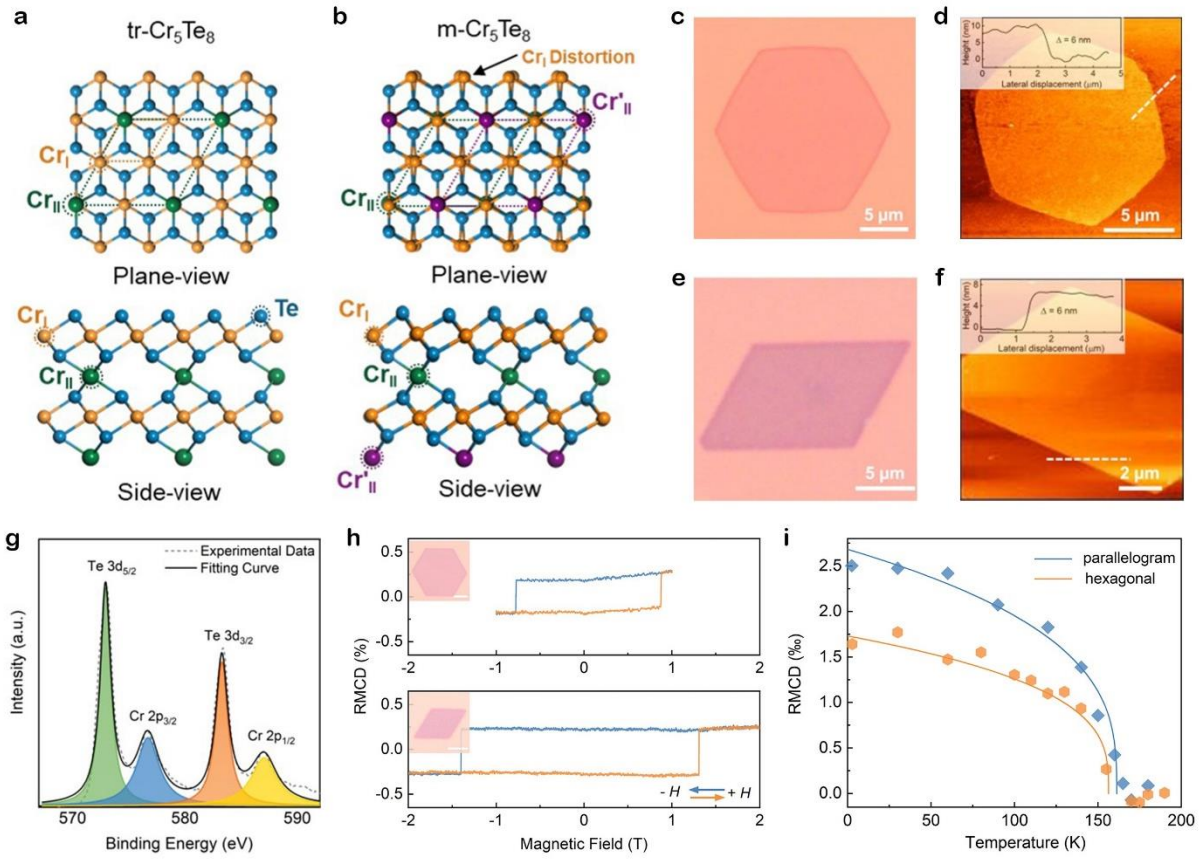

Fig. 1 | Synthesis and characterizations of 2D tr-Cr_5Te_8 and m-Cr_5Te_8. a,b, Crystal structure of tr-Cr_5Te_8 (**a**) and m-Cr_5Te_8 (**b**) crystals along different axes, respectively. **c,d**, OM (**c**) and AFM (**d**) images of the hexagonal tr-Cr_5Te_8 flake. **e,f**, OM (**e**) and AFM (**f**) images of the parallelogram m-Cr_5Te_8 flake. **g**, High-resolution XPS spectra of Cr 2*p* and Te 3*d* of Cr_5Te_8. **h**, Polar RMCD signals of the tr-Cr_5Te_8 and m-Cr_5Te_8 measured at 2.5 K. The insets are the corresponding optical images. Scale bar, 5 μm. **i**, Remanent RMCD signals of Cr_5Te_8 at zero magnetic field as a function of temperature obtained from the datasets shown in Supplementary Fig. 7.

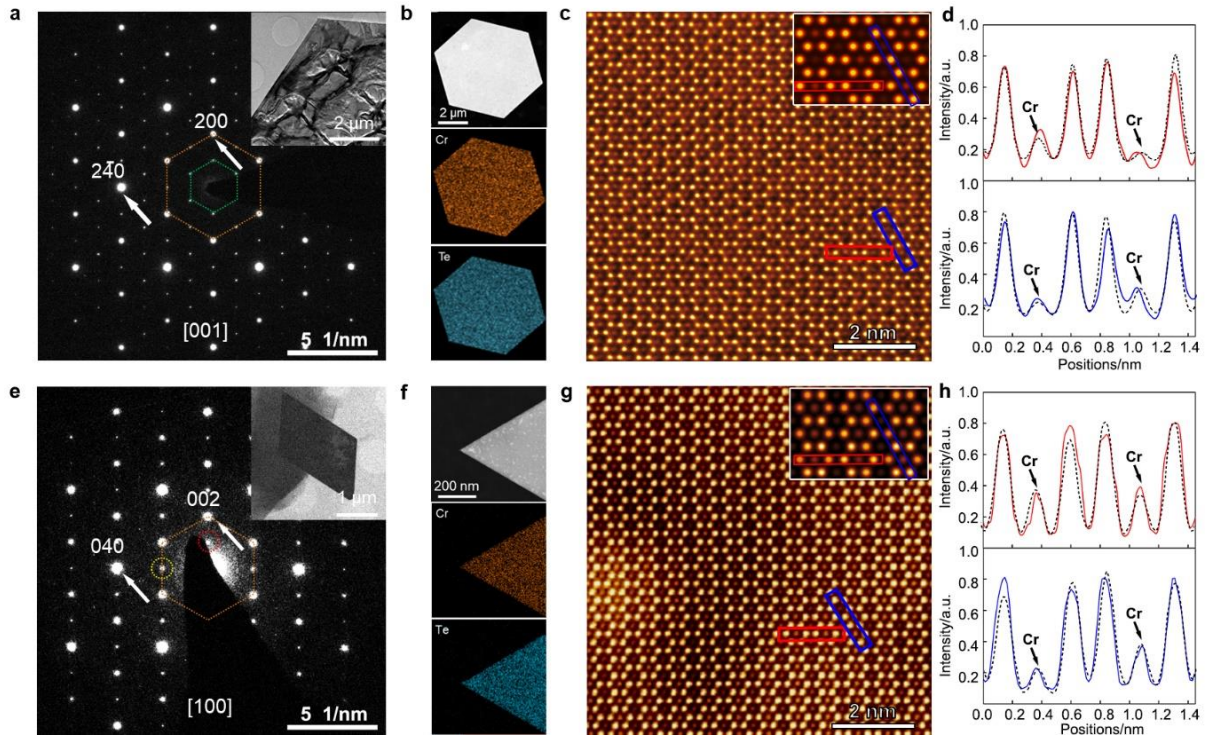

Fig. 2 | Atomic morphology of tr-Cr_5Te_8 and m-Cr_5Te_8 crystals. a,**e**, Diffraction pattern of tr-Cr_5Te_8 (**a**) and m-Cr_5Te_8 (**e**) crystals, respectively. The upper right inset in each image is the corresponding bright-field image. **b**,**f**, HAADF and corresponding EDS mapping of tr-Cr_5Te_8 (**b**) and m-Cr_5Te_8 (**f**) crystals, respectively. **c**,**g**, Atomically resolved HAADF-STEM image of tr-Cr_5Te_8 (**c**) and m-Cr_5Te_8 (**g**) crystals, respectively. The upper right inset is the corresponding simulated STEM annular dark-field image. **d**,**h**, Intensity line profiles for the red and blue rectangles marked in **c** and **g**, respectively. The black dotted lines represent the corresponding intensity line profiles of simulated STEM images.

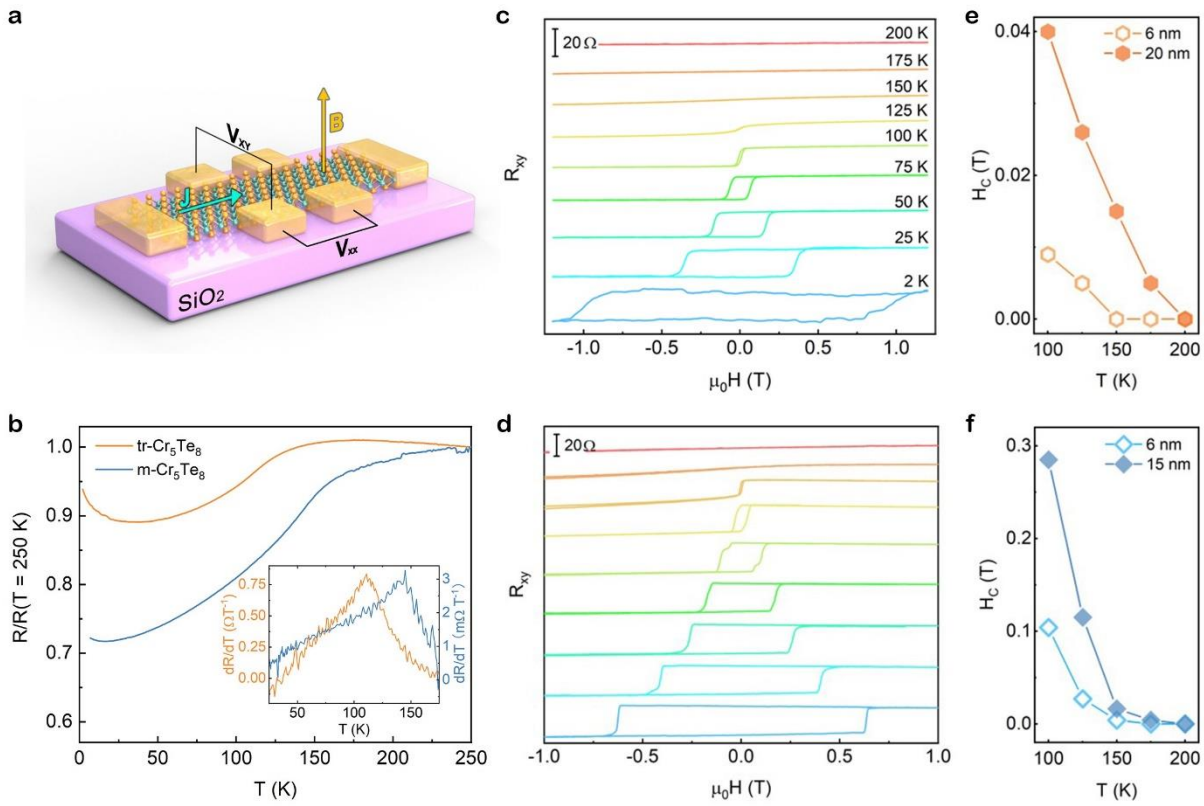

Fig. 3 | Magnetotransport measurement of 2D Cr_5Te_8. a, Schematic illustration of the Hall bar device. **b**, Temperature dependence of the longitudinal resistance (R) of tr-Cr_5Te_8 and m-Cr_5Te_8 with the thickness of 6 nm, respectively. Resistances are normalized by their values at T = 250 K. The bottom-right inset shows the first derivative of the longitudinal resistance as a function of temperature. The red arrow shows there the ferromagnetic-paramagnetic transition occurs. **c,d**, Temperature-dependent magnetic field (out-of-plane) sweeps of the Hall resistance measured on the 6 nm thick tr-Cr_5Te_8 device (**c**) and 6 nm thick m-Cr_5Te_8 device (**d**), respectively. **e,f**, The coercivity fields of the tr-Cr_5Te_8 devices (**e**) and m-Cr_5Te_8 devices (**f**) with different thicknesses, as a function of temperature.

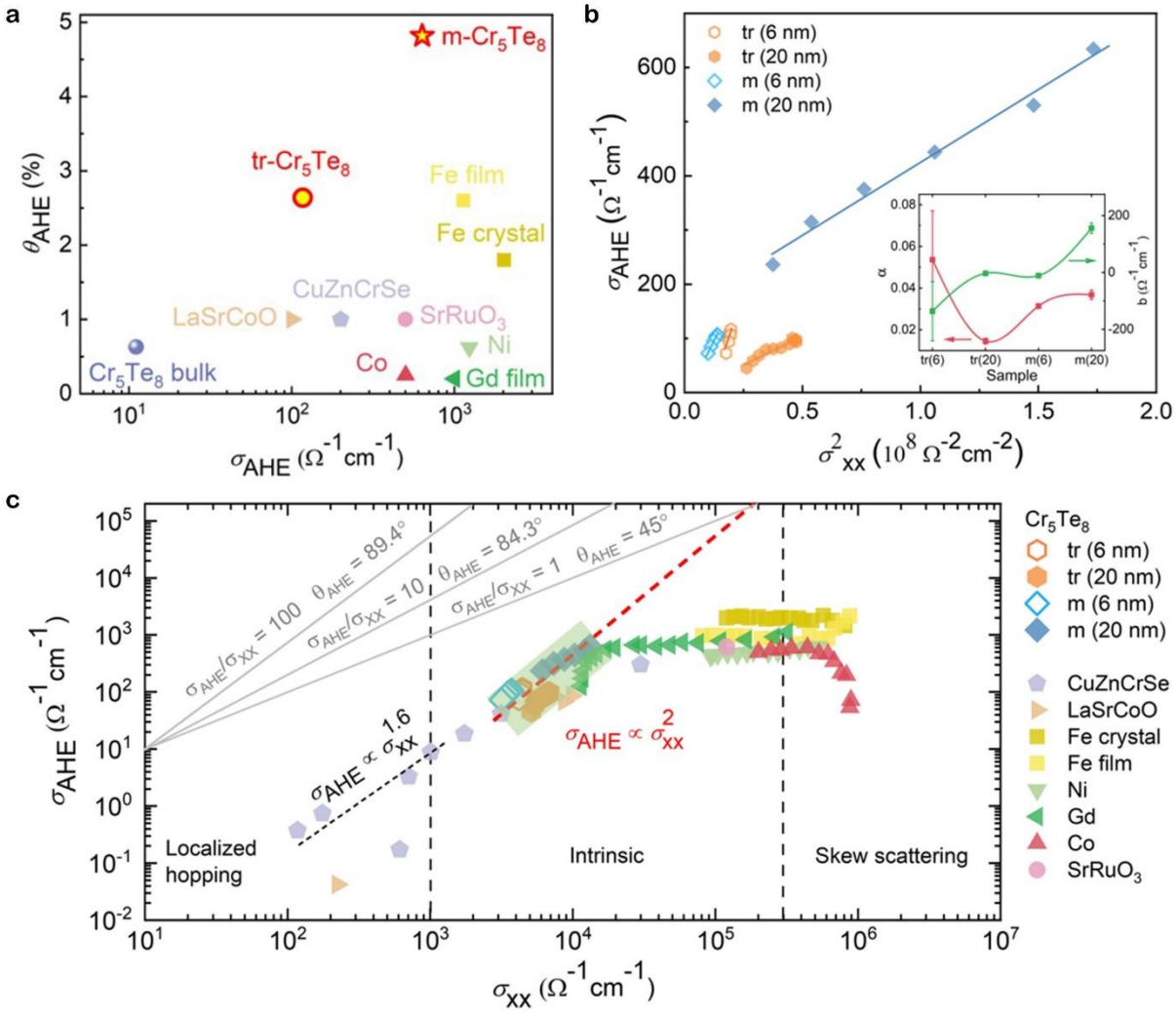

Fig. 4 | AHE of 2D Cr_5Te_8 and other metallic ferromagnets. a, Comparison of the anomalous Hall conductivity and anomalous Hall angle of our Cr_5Te_8 with other metallic ferromagnetic materials. **b**, Extracted σ_{AHE} versus σ^2_{xx} for the Cr_5Te_8 samples covering different phases and thicknesses. Solid lines are fittings to the equation shown in the inset to extract the skew scattering constant (α) and intrinsic σ_{AHE} (b) for each sample, which are summarized in the inset. **c**, Full logarithmic plot of σ_{AHE} versus σ_{xx} for all the materials discussed in **a**, spanning from the dirty regime to the extrinsic regime.

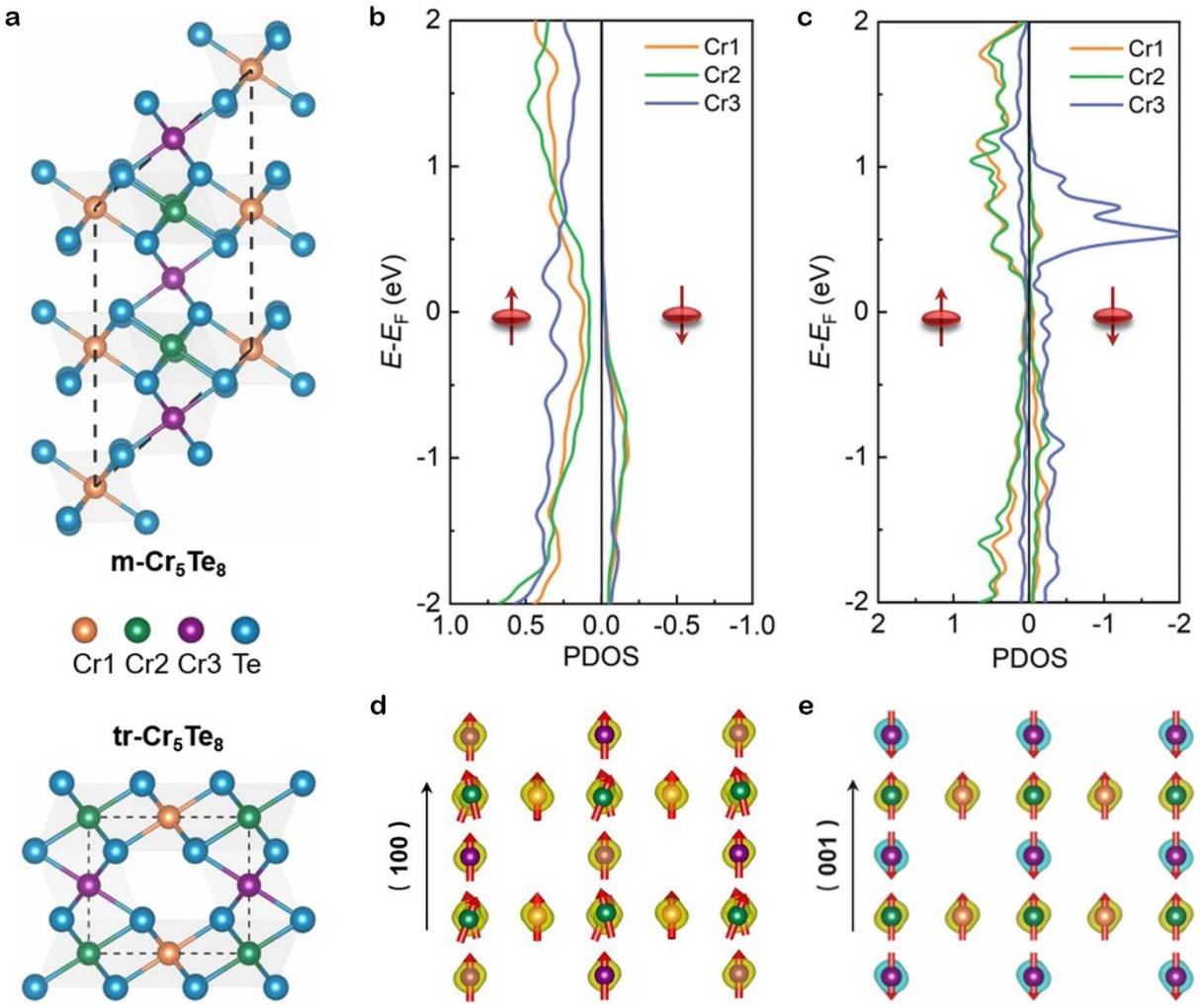

Fig. 5 | Atomic structures and magnetism of Cr_5Te_8. a, Side views of the m-Cr_5Te_8 (top) and tr-Cr_5Te_8 (bottom). The crystalline lattices are highlighted by dashed lines. Three types of Cr atoms are colored in orange, green and purple, respectively, and the Te atoms are colored in blue. **b,c**, The Cr-projected spin-polarized DOS of total *d* orbitals of m-Cr_5Te_8 (**b**) and tr-Cr_5Te_8 (**c**), respectively. The spin-up states and spin-down states are indicated by the red arrows. **d,e**, The spin ordering of m-Cr_5Te_8 (**d**) and tr-Cr_5Te_8 (**e**) indicated by red arrows. The noncollinear spin ordering in m-Cr_5Te_8 stems from the structural distortion. The spin-up and spin-down component of the spin-polarized electron density on Cr atoms are coloured in yellow and cyan with isosurface value of 0.05$Å^{-3}$.